X-ray absorption measurements on nickel cathode of sodium-beta alumina batteries: Fe–Ni–Cl chemical associations

Mark E. Bowden [a], Kyle J. Alvine [a], John L. Fulton [a], John P. Lemmon [a], Xiaochuan Lu [a], Bobbie-Jo Webb-Robertson [a], Steve M. Heald [b], Mahalingam Balasubramanian [b], Devon. R. Mortensen [c], Gerald T. Seidler [c], Nancy J. Hess [a],*

[a] Pacific Northwest National Laboratory, P.O. Box 999, Richland, WA 99352, USA
[b] Advanced Photon Source, Argonne National Laboratory, 9700 South Cass Ave., Argonne, IL 60439, USA
[c] University of Washington, Department of Physics, Box 351560, Seattle, WA 98195, USA

HIGHLIGHTS

- X-ray spectroscopy is used to study elemental correlations in sodium–nickel chloride batteries.
- Temperature and charge state had the most significant impact on Ni–Fe correlations.
- Fe additive was present either as Fe metal or an Fe(II) chloride.

ABSTRACT

Sections of Na–Al–NiCl$_2$ cathodes from sodium-beta alumina ZEBRA batteries have been characterized with X-ray fluorescence mapping, and XANES measurements to probe the microstructure, elemental correlation, and chemical speciation after voltage cycling. Cycling was performed under identical load conditions at either 240 or 280 °C operating temperature and subsequently quenched in either the charged or discharged state. X-ray fluorescence mapping and XANES measurements were made adjacent to the current collector and β″-Al$_2$O$_3$ solid electrolyte interfaces to detect possible gradients in chemical properties across the cathode. An FeS additive, introduced during battery synthesis, was found to be present as either Fe metal or an Fe(II) chloride in all cathode samples. X-ray fluorescence mapping reveals an operating temperature and charge-state dependent spatial correlation between Fe, Ni, and Cl concentration. XANES measurements indicate that both Ni and Fe are chemically reactive and shift between metallic and chloride phases in the charged and discharged states, respectively. However the percentage of chemically active Ni and Fe is significantly less in the cell operated at lower temperature. Additionally, the cathode appeared chemically homogeneous at the scale of our X-ray measurements.

© 2013 Elsevier B.V. All rights reserved.

1. Introduction

Renewable energy generation systems and energy storage devices have gained a great deal of attention in the past few decades due to the negative environmental impacts of the burning of fossil fuels [1–5]. The ideal requirements for the energy storage devices or batteries are high energy density, medium to high power density, long cycle life, low cost and safe operation. One such potential storage technology is the sodium-beta battery (NBB), which is based on a molten sodium anode and β″-Al$_2$O$_3$ solid electrolyte (BASE) [6–9]. NBBs reversibly store and release electrical energy via sodium ion transport across the BASE between a positive and negative electrode. Two types of NBBs, distinguished by cathode materials, have been widely studied, namely the sodium-sulfur (Na–S) battery and sodium-metal halide (ZEBRA) batteries.

The Na–S battery is typically operated at high temperatures (e.g. 300–350 °C) with molten sulfur as the cathode [7,8]. The electrochemical reaction for Na–S battery is as follows:

$$xS + 2Na^+ + 2e^- \Leftrightarrow Na_2S_x (x = 3 - 5), E = 2.08 \text{ to } 1.78 \text{ V at } 350 \text{ °C} \tag{1}$$
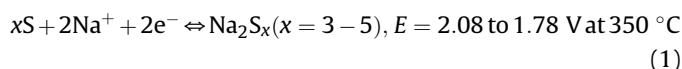
The Na–S chemistry offers several attractive features, such as high (theoretical) energy density (∼760 Wh kg^{-1}), high-energy

* Corresponding author. Tel.: +1 509 371 6385; fax: +1 509 371 6354.
 E-mail address: nancy.hess@pnnl.gov (N.J. Hess).

efficiency, and good cycle life. Here, the battery is primarily comprised of alumina, sulfur and sodium, which are relatively non-toxic, inexpensive and readily available. The combination of these features makes the Na–S chemistry extremely attractive compared to other technologies such as lithium-ion, Ni-metal hydride, or Pb-acid batteries for grid-scale electrical energy storage. Drawbacks of the Na–S battery technology include: (1) intrinsic corrosive behavior of polysulfide melts, which limits material selections for both cathode current collector and battery casing; (2) safety issue and open-circuit cell failure mode. If the BASE is broken during battery operation, molten sulfides may come in direct contact with molten sodium and the resulting reactions are inherently vigorous. This could potentially result in a fire and even explosion since the battery operation temperature is relatively close to boiling point of sulfur (440 °C). Neighboring cells may also be affected by such an event and this could result in severe power loss due to open circuit [8].

An alternate type of NBB is the ZEBRA (ZEolite Battery Research Africa) battery, in which transition metal halides such as $NiCl_2$, $FeCl_2$ and $ZnCl_2$ are used as active materials in the cathode [10–15]. ZEBRA batteries typically need a molten secondary electrolyte such as $NaAlCl_4$ (melting point of 157 °C) to ensure facile sodium ion transport between the BASE and solid cathode materials. The electrochemical reaction of Na–$NiCl_2$ cell follows:

$$NiCl_2 + 2Na \Leftrightarrow Ni + 2NaCl, \ E \ = \ 2.58 \ \text{V at } 300 \ °C \quad (2)$$
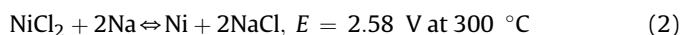
ZEBRA batteries exhibit a number of advantages over the Na–S battery, which include: higher voltage (~ 0.5 V higher), ease of assembly in discharged state, less corrosive nature of cathode materials, lower operating temperature (~ 50 °C lower), safer cell failure mode, and better tolerance against overcharging [8]. One notable disadvantage of the current ZEBRA technologies is lower energy density as compared to the Na–S battery technology. A successful strategy to compensate for the lower energy density is to adopt a planar or "button cell" geometry, as shown in Fig. 1. This geometry results in higher power and energy density compared to a tubular battery due to the thin cathode and large active interfacial areas between the battery components [16].

Among various transition metal halides, Ni/$NiCl_2$ is one of the most popular choices for ZEBRA battery cathode due to the simple cell chemistry, high open circuit voltage, and relatively high electrochemical stability with the $NaAlCl_4$ melt and BASE [17]. However, performance degradation with cycling has prevented widespread deployment. Performance degradation of Na–$NiCl_2$ battery has been primarily linked to microstructure changes, namely the growth and progressive coarsening of Ni and NaCl particles within the cathode [11,15,16]. Coarsening of Ni particles within the cathode leads to increased cathode polarization

resistance and fade in cell performance during voltage cycling due to the reduction in net active surface area, which effectively reduces the number of electrochemical reaction sites [15,18]. Previous work [15,17] has shown that Ni grain coarsening is a significant factor at elevated temperatures but a recent study [20] has shown that at temperatures as low as 265 °C the growth of a NaCl capping layer on Ni grains appeared to be the dominant factor in decreased battery performance.

The incorporation of chemical additives such as NaBr, NaI, S, Al, Fe, and FeS during cathode synthesis has been shown to suppress Ni grain growth or otherwise enhance battery performance [11,19–21] although the detailed mechanisms by which these additives modify the cathode chemistry are not well understood. Sudworth [22] has summarized the current understanding as follows: it is thought that that halide additives stabilize the resistance of the battery, the addition of Al powder assists in the formation of dispersed $NaAlCl_4$ regions within the cathode increasing battery performance, whereas S suppresses Ni grain growth by poisoning the Ni surface. Less is known about the role of Fe in ZEBRA battery chemistry. At high concentrations, Fe provides high peak power capability and prevents overdischarge damage to the cell [22] due to its lower electrochemical potential in the reaction:

$$FeCl_2 + 2Na \Leftrightarrow Fe + 2NaCl, \ E \ = \ 2.35 \ \text{V} \quad (3)$$
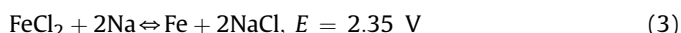
The role of the Fe additive at relatively low concentrations remains undetermined.

In this paper, several X-ray techniques were used to map the elemental association and chemical speciation of Ni, Fe and Cl chemical components of the Na–$NiCl_2$ cathode of batteries operated at 240 or 280 °C for 25 cycles each with 2 wt % FeS additive. The 240 °C and 280 °C cycling temperatures were chosen because previous studies [15,23] had found that the performance of the cell at these temperatures was quite similar but nonetheless different. One objective of this study is to investigate the subtle changes in battery chemistry that may underlie the subtle differences in performance. Supporting microscopy and EDS were also carried out. We find that operating temperature and state of charge have significant impact on the Fe–Ni and Fe–Cl elemental associations. The chemical speciation, or presence of Ni and Fe metal or chloride, is largely determined by operating temperature and state of charge. Additionally, the presence of Ni or Fe metal showed a weak correlation with its respective elemental concentration. No consistent difference in chemical properties were observed in regions sampled near the BASE and cathode interfaces suggesting that the cathodes are homogeneous at the scale of our X-ray measurements. The results of this study illustrate the value of these X-ray techniques for mechanistic investigations of the impact of low concentrations of additives on battery chemistry and performance.
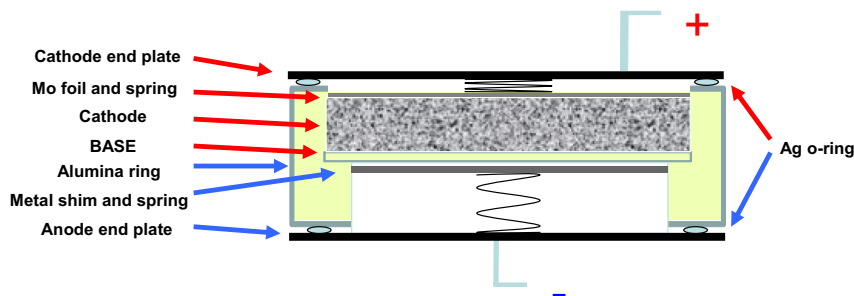

Fig. 1. Simplified schematic of the Ni button battery cross-section. Modified from Lu et al. [22].

2. Experimental

2.1. Battery fabrication and testing

BASE discs were prepared using a vapor phase conversion process starting with powders of high purity α-Al_2O_3 (Almatis, >99.8%) and yttria-stabilized zirconia (UCM Advanced Ceramics, 8 wt% yttria-stabilized zirconia), as described previously [8,15–17]. α-Al_2O_3/YSZ discs were fabricated via a tape-casting technique and were fired at 1600 °C in air to achieve full density (>99%). The sintered α-Al_2O_3/YSZ discs were then placed in loose β''-Al_2O_3 powder and heat-treated at 1450 °C in air in order to convert α-Al_2O_3 into β''-Al_2O_3. The thickness of the converted composite β''-Al_2O_3/YSZ discs was ~600 μm.

A schematic of a ZEBRA battery in button cell geometry is shown in Fig. 1 [24]. A BASE disc was glass-sealed to an α-Al_2O_3 ring (active cell area: ~3 cm^2). It was then moved into an argon-filled glove box. One gram of cathode granules consisting of Ni, NaCl and small amounts of additives (1–2 wt. % each of FeS, NaF, NaI, Al) was loaded into the cathode chamber of the cell. After the granules were dried at 270 °C under vacuum to remove of moisture, molten $NaAlCl_4$ secondary electrolyte was infiltrated into the cathode. A foil and a spring made of Mo were placed on the top of the cathode as a current collector. A spring-loaded stainless steel shim, which served as a molten sodium reservoir, was then inserted into the anode compartment. Anode and cathode end plates were then compression-sealed to both sides of α-Al_2O_3 ring using gold o-rings. Nickel leads, which served as current collectors, were welded to the electrode end plates.

The assembled cell was then heated in air to 280 °C, at which point, it was then charged to 2.8 V under a constant current of 10 mA. This initial charging produces $NiCl_2$ in the cathode necessary for battery operation. The cell was then discharged back to 80% of the starting charge capacity using the same initial current. After the initial cycle, the cell was voltage cycled between 20 and 80% of the initial charge capacity at a constant operating temperature (280 or 240 °C depending on the battery) under a constant current of 90 mA, which corresponded to 1 C rate for the cycling capacity of 90 mAh. The voltage was restricted to limits of 2.8 and 1.8 V in order to avoid overcharging and over-discharging, respectively, using a BT-2000 Arbin Battery Testing system. All battery samples were cycled 25 times to induce moderate degradation for these studies; though it should be noted that typical ZEBRA battery lifetimes are on the order of thousands of cycles [8,11]. At 280 °C no capacity fade is observed, while at 240 °C there is a capacity loss of approximately 50 mAh consistent with our earlier studies [15]. The capacity fade at 240 °C results from the use of the same current (90 mA) both temperatures. The cycled batteries were then quenched to room temperature in either the charged or the discharged state, depending on the sample. Battery sample names, cycling conditions, and state of charge are summarized in Table 1. The battery sample names HC and HD designate battery samples cycled at 280 °C and quenched in charged and discharged states, respectively, whereas LC and LD refer to battery samples cycled at 240 °C and quenched in the charged and discharged states, respectively.

Table 1
Battery sample conditions.

Sample	Temperature [°C]	State	Voltage range [V]	Load [mA]	Cycles
HC	280	Charged	1.8–2.8	90	25
HD	280	Discharged	1.8–2.8	90	25
LC	240	Charged	1.8–2.8	90	25
LD	240	Discharged	1.8–2.8	90	25

2.2. Cathode sectioning for SEM and XAS

Sectioned samples from the cathodes were prepared for SEM and X-ray analysis using standard cross-sectioning techniques in an Ar filled glove box. The Na–$NiCl_2$ cathode was sectioned to expose a portion of the cathode spanning the BASE to current collector. These sections were embedded in epoxy, cut into thin sections and polished to approximately 10 μm in thickness under oil to mitigate air and moisture exposure. Residual cutting oil was removed with acetone and the samples were immediately transferred to an Ar filled desiccator. The granular nature of these cathode subsections precluded further thinning to form sub 10 μm wedges, which would be ideal for transmission X-ray measurements. Instead, X-ray fluorescence and near edge X-ray absorption measurements were performed as detailed section 2.4.

2.3. SEM/EDS measurements

Regions of the HC and HD samples adjacent to the BASE interface were analyzed using a scanning electron microscope (SEM, JEOL, JSM-7600F) with an Oxford X-Max 80 mm^2 drift energy dispersive detector prior to synchrotron-based X-ray studies. The operating voltage for the Electron Dispersive Spectroscopy (EDS) was 10 kV and corresponding spot current of nominally 6 nA. Due to the penetration and multiple scattering of the electron beam within the sample the EDS measurements have an approximate lateral resolution on the order of 1–2 μm. Additionally, although EDS measurements are influenced by subsurface features it still yields important compositional information about features identified in the SEM image.

2.4. X-ray studies

X-ray Absorption Spectroscopy can provide a wealth of quantitative information about the concentration, oxidation state, and coordination environment bound to the absorbing element. X-ray Absorption Near Edge Structure (XANES) measurements and X-ray Fluorescence Maps (XFM) of the ZEBRA cathode sections were performed at sector 20 bending magnet beamline (20BM) of the Advanced Photon Source (APS), Argonne National Laboratory. Within each of the four cathode samples described above, regions of interest located within approximately 50 μm of the BASE or current collector interface were selected for analysis. The X-ray beam was collimated to a spot size of approximately 5 μm × 5 μm using a pair of Kirkpatrick–Baez focusing mirrors and yielded relatively high lateral resolution with an incident flux of approximately 10^9 photons/s.

2.4.1. X-ray fluorescence mapping

For XFM measurement, the cathode sections were measured in a standard fluorescence geometry with the sample face placed at 45° to the incident beam (polarized in the horizontal direction) and an energy dispersive silicon drift detector (VORTEX) at 90° to minimize the contribution from elastic scatter. The XFM were collected with the incident X-ray energy at 8.352 or 9.700 keV, above the Cl, Fe and Ni absorption K-edges at 2.822, 7.112, and 8.333 keV, respectively, allowing for simultaneous collection of Cl, Fe, and Ni XFMs. All fluorescence intensities were normalized by the incident X-ray intensity corrected for deadtime. XFM could be collected over 220 × 220 μm area with a 5 μm step-size in approximately 90 min.

Due to the high concentration of Ni in the battery sample relative to Fe and Cl, we assessed the potential influence of the Ni signal on the adjacent Fe and Cl peaks. Our analysis showed that while the tail of the Ni peak did partially overlap with the Fe peak, the integrated counts was on the order of 1% or less for the Fe
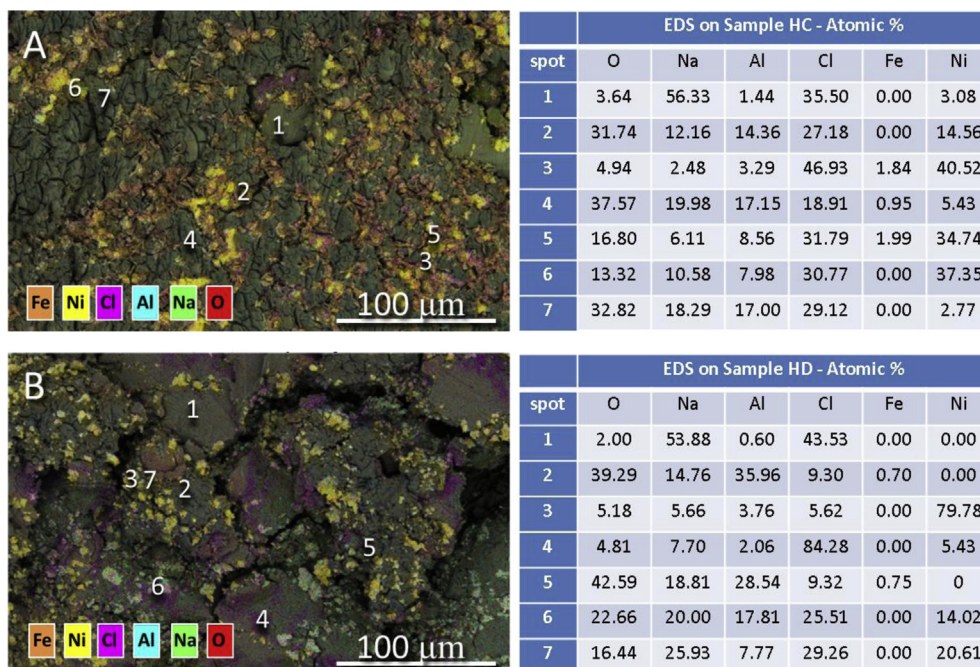
EDS on Sample HC - Atomic %						
spot	O	Na	Al	Cl	Fe	Ni
1	3.64	56.33	1.44	35.50	0.00	3.08
2	31.74	12.16	14.36	27.18	0.00	14.56
3	4.94	2.48	3.29	46.93	1.84	40.52
4	37.57	19.98	17.15	18.91	0.95	5.43
5	16.80	6.11	8.56	31.79	1.99	34.74
6	13.32	10.58	7.98	30.77	0.00	37.35
7	32.82	18.29	17.00	29.12	0.00	2.77

EDS on Sample HD - Atomic %						
spot	O	Na	Al	Cl	Fe	Ni
1	2.00	53.88	0.60	43.53	0.00	0.00
2	39.29	14.76	35.96	9.30	0.70	0.00
3	5.18	5.66	3.76	5.62	0.00	79.78
4	4.81	7.70	2.06	84.28	0.00	5.43
5	42.59	18.81	28.54	9.32	0.75	0
6	22.66	20.00	17.81	25.51	0.00	14.02
7	16.44	25.93	7.77	29.26	0.00	20.61

Fig. 2. SEM images of HC and HD samples colorized with EDS information. The color codes are in the lower left corner and indicate regions of higher concentration for the particular elements. (A) is an image from a section of sample HC, and (B) is an image from a section of sample HD. Ni particles can be seen as bright yellow regions. Black regions are microcracks in the material. To the right of each image is a table of the relative atomic concentrations of specific points shown in each image for the O, Na, Al, Cl, Fe, and Ni. Concentrations are normalized to 100%. (For interpretation of the references to color in this figure legend, the reader is referred to the web version of this article.)

concentrations observed. The contribution to the Cl signal was even lower as the energy separation was larger for that peak. The XFM data was utilized to visualize the spatial distribution of Cl, Fe, and Ni and to determine Fe–Ni and Fe–Cl concentration correlations through statistical analysis. Using statistical analysis we compared the Fe–Ni and Fe–Cl correlation for the top 25% of Fe abundant regions and bottom 25% of Fe abundant regions for each map. We defined Fe-abundant regions as those with the top 25% of Fe concentration, and Fe-poor regions as the lowest 25%. However, prior to this calculation we removed data points where the X-ray absorbance, $\log(I_0/I_T)$ where I_0 is the incident X-ray beam intensity and I is the intensity of the transmitted X-ray beam, was less than 0.8 to minimize possible sample thickness effects even though fluorescence measurements are believed insensitive to sample thickness. The correlation is based upon a standard Pearson correlation calculation. To evaluate if the correlation is significant we test the null hypothesis that $R = 0$ using a standard t-test.

2.4.2. X-ray absorption near edge spectroscopy

Individual Ni XANES spectra were obtained at selected points based on the elemental maps, and took approximately 10 min to acquire at each location. The low concentration of Fe in these samples required approximately 30 min per location to acquire Fe XANES spectra with comparable signal to noise ratio. As a result, fewer Fe XANES spectra were collected from each sample. Ni and Fe metal foils were measured to calibrate the incident X-ray energy prior to each XANES or Extended X-ray Absorption Fine Structure (EXAFS) scan. Ni, NiO, Ni_3S_2, $NiCl_2$, Fe, Fe_2O_3, $FeCl_3$, and FeS samples were also measured as standards for later identification of Ni and Fe species within the battery. The collected XANES spectra were used to track the evolution of the Ni and Fe oxidation states in a spatially resolved manner across the cathode. XANES spectra were fit with linear combinations of standards spectra using the Athena program [25]. No self-absorption corrections were used since both the samples and standards exhibited similar geometry and thickness.
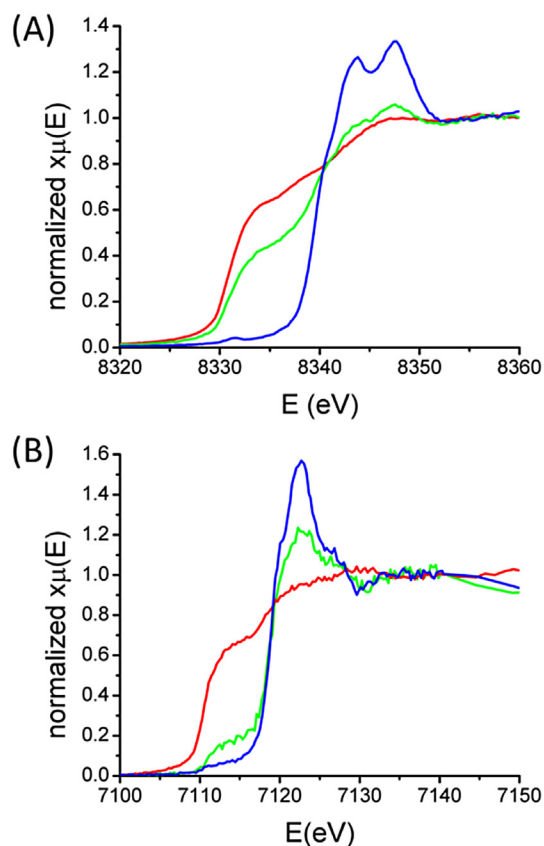

Fig. 3. Representative XANES absorbance spectra from the Na–NiCl$_2$ cathode compared to standards spectra for Ni (A) and Fe (B). In each figure, the cathode spectra is the green curve, the Fe or Ni metal is the red curve, and the NiCl$_2$ or the (presumed) Fe(II) chloride is given by the blue curve. The cathode spectra are fit with linear combinations of the metal and chloride spectra. (For interpretation of the references to color in this figure legend, the reader is referred to the web version of this article.)

Data were normalized to the pre and post edge before linear combination fitting.

All Ni species XANES spectra were fit with a linear combination of Ni metal and $NiCl_2$ XANES as shown in Fig. 3A, to estimate the Ni oxidation state at a measurement spot. EXAFS data taken (not shown), support the assertion that Ni in the cathode material is present as either Ni metal or $NiCl_2$. The Fe XANES spectra similarly appear to be a linear combination of Fe metal and one other "unknown" chemical species as indicated by an isosbestic (crossover) point when plotting all of the Fe spectra from the different samples on the same axis. The spectrum of the "unknown" Fe species was characterized by a strong "white line" at 7122 eV as shown in Fig. 3B, and identified as an Fe(II) chloride, most probably $FeCl_2$ or Na_6FeCl_8, on the basis of literature comparisons and previous reports of these compounds in iron-containing ZEBRA batteries (see Supplemental information). Our data was not able to distinguish between these candidate compounds which both contain Fe(II) octahedrally coordinated to Cl with similar bond distances.

To provide a standard for linear combination fitting, several similar Fe spectra from the cathode samples with the strongest white line were averaged to create a Fe(II) chloride "standard". An example Fe cathode spectrum and its corresponding fit are shown in Fig. 3B. All spectra gave similarly good fits and thus we assume that Fe is present in the cathode material either as Fe metal or Fe(II) chloride and similarly assume that the Fe oxidation state can be estimated from linear combinations. This approach could give as high as a $\pm 15\%$ uncertainty in the Fe oxidation state determination, which is acceptable to draw general correlations and conclusions in this study.

2.4.3. Two dimensional XANES mapping

XANES analyses provide very useful information on the elemental chemical speciation, such as the oxidation state; but collection of the full XANES spectrum for a spatial map would be time prohibitive using traditional approaches. We applied an X-ray absorption imaging technique similar to that developed by Pickering et al. [25] for biological samples. For this XANES mapping technique, we identified two specific energies in the Ni XANES spectra at which the intensity value is highly dependent on the Ni chemical species present (8347 eV) and a second reference energy (8352 eV) at which the intensity was independent of Ni species. The X-ray beam is rastered over the sample area twice, once at each of the two energies. An approximate map of the $NiCl_2$ distribution is then generated by taking the ratio of the two intensities at each point.

3. Results and discussion

3.1. SEM/EDS

Representative SEM images of the cathode sections cycled at 280 °C in the charged and discharged state (samples HC and HD), are shown in Fig. 2A and B, respectively. These images are colorized based on EDS data for regions of high concentration of each of the following: Fe, Ni, Cl, Al, Na, and O. Although not reported, S was also detected but at such low levels as not be quantifiable. Bright yellow and orange regions, approximately 7–10 μm in diameter, are Ni and $NiCl_2$ grains, respectively. These
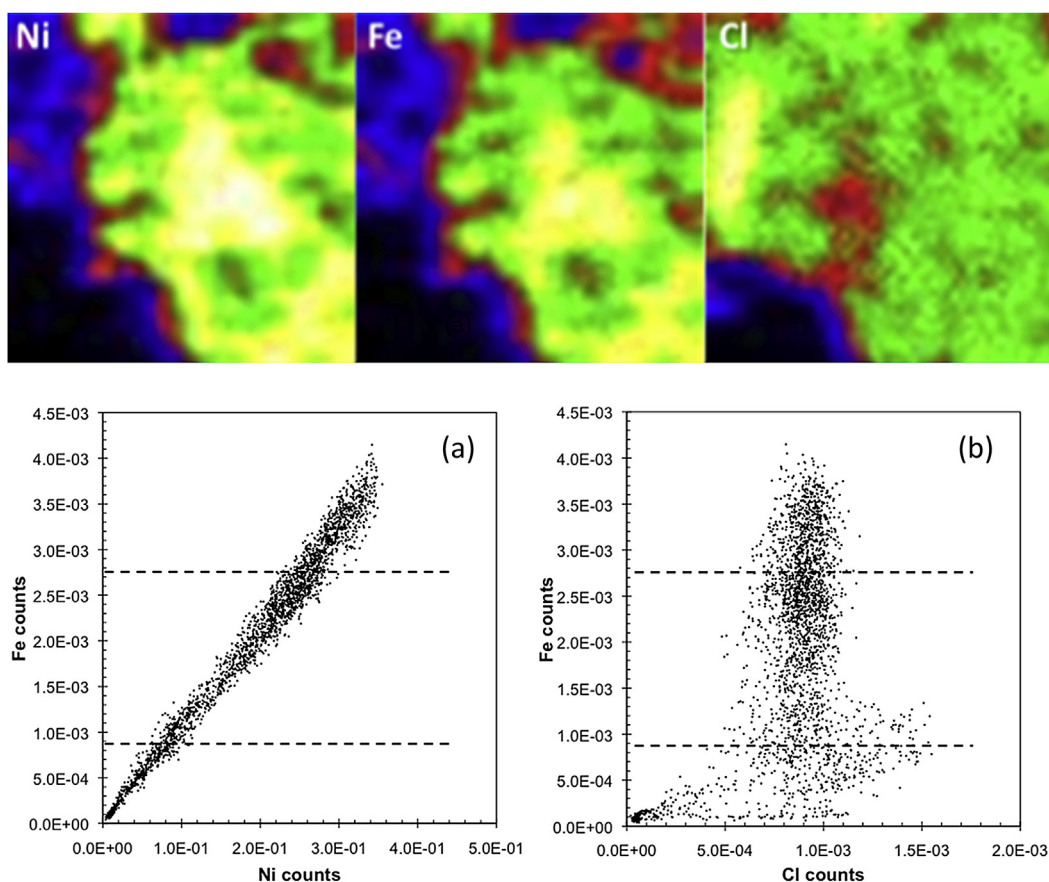

Fig. 4. XFM of HC cathode (280 °C, charged) adjacent to BASE interface. The Ni, Fe, and Cl XFM are labeled correspondingly. White and black colors indicate high and low elemental concentrations, respectively. Each map is 200 μm × 200 μm. The correlations between the Fe–Ni and Fe–Cl fluorescence signals are shown in graphs (a) and (b), respectively. Each point on the graph represents the composition of one 5 μm × 5 μm pixel in the XFM.

bright regions are less abundant in the SEM image of HD (discharged state, Fig. 2B) and instead diffuse magenta regions, indicating high Cl concentrations, are evident. Fig. 2 also includes tables of normalized atomic concentrations measured at specific points labeled in the SEM image.

3.2. X-ray studies

3.2.1. X-ray fluorescence mapping (XFM)

Analyses of Ni, Fe, and Cl XFM maps allow qualitative assessment of the effect of the state of charge, operating temperature, and proximity to the BASE interface on chemical state of Ni and Fe in the cathode. Due to the 5 micron spot size of the X-ray beam we were unable to detect chemical gradients within smaller single particles of the Ni cathode. Comparison of charged and discharged states of cathodes operated at the same temperature (i.e., HC vs. HD and LC vs. LD) permits insight into the chemical processes operating during cycling. Comparison of cells cycled at 280 °C (HC, HD) to cells cycled at 240 °C (LC, LD) were used to assess the effect of operating temperature on cathode degradation through changes in chemical speciation. Lastly, because the cell was cycled between 20 and 80% of the initial charge capacity, the cathode adjacent to the BASE represents a more chemically active area of the cathode compared to the current collector location [22]. Ni, Fe, and Cl XFM of the cathode samples HC, and HD collected near the BASE interface are shown in Figs. 4 and 5, respectively. Corresponding maps from the LC and LD samples are shown in Figs. 6 and 7. Analogous maps for regions near the current collector can be found in the Supplemental information.

Visual examination of the XFM images provides qualitative assessment of Fe, Cl, and Ni elemental correlation. In order to perform a more quantitative assessment of the elemental associations we used statistical methods to answer two questions: 1) is Fe spatially correlated with either Ni or Cl across the sample, and 2) does the observed correlation change if only the most Fe abundant regions are considered?

The Fe counts for each measurement point were plotted as a function of either Ni or Cl counts at the same spatial location (Figs. 4 and 5), providing a quick visual indication of whether the Fe concentration at individual points was correlated with Ni or Cl concentration. The horizontal dotted lines in these graphs delineate the Fe-abundant and Fe-poor data, allowing an assessment of whether the correlations are different in these regions. Tables 2 and 3 summarize the Pearson correlation results for the Fe–Ni and Fe–Cl comparisons respectively, separated into the Fe-abundant and Fe-poor regions. The correlation values with corresponding p-values of less than 0.05 are considered significant based on a Bonferroni multiple test correction [26]. Non-significant correlation values are shown in italics in Tables 2 and 3 Analogous statistical analysis of data collected near the current collector interface can found in the Supplemental information. Because the BASE end of the cathode is thought to be more chemically active than the current collector end [22], only the sample locations near the BASE interface will be discussed for the evaluation of the state of charge and operating temperature effect.

3.2.1.1. State of charge.
The impact of the charge state on the Fe–Ni elemental distribution in the high temperature samples (HC in
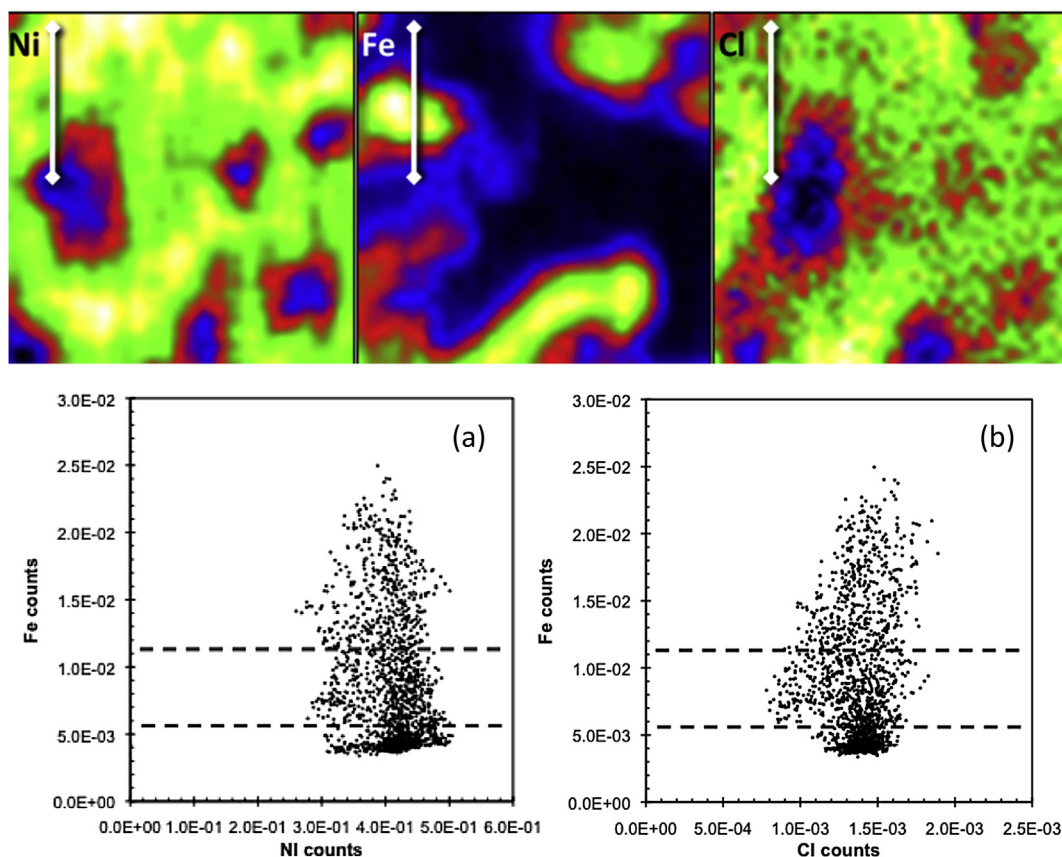

Fig. 5. XFM of HD cathode (280 °C, discharged) adjacent to BASE interface. The Ni, Fe, and Cl XFM are labeled correspondingly. White and black colors indicate high and low elemental concentrations, respectively. Each map is 200 μm × 200 μm. The correlations between the Fe–Ni and Fe–Cl fluorescence signals are shown in graphs (a) and (b), respectively. Each point on the graph represents the composition of one 5 μm × 5 μm pixel in the XFM.
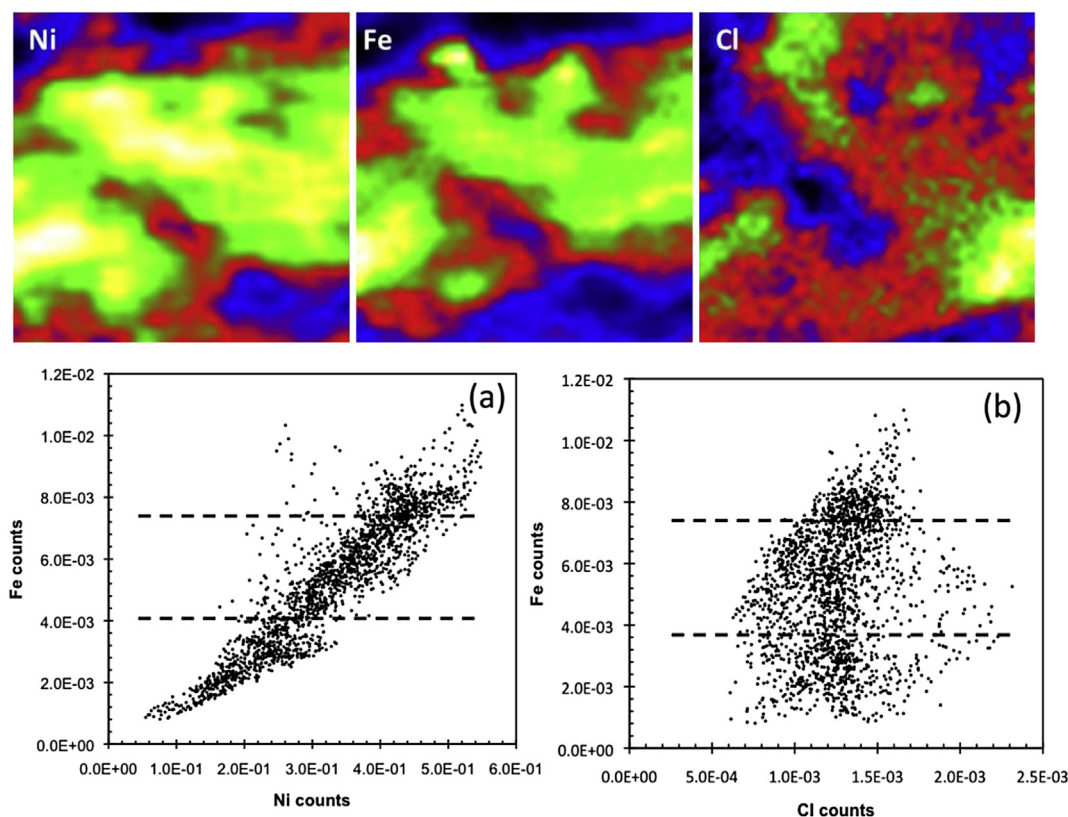
Fig. 6. XFM of LC cathode (240 °C, charged) adjacent to BASE interface. The Ni, Fe, and Cl XFM are labeled correspondingly. White and black colors indicate high and low elemental concentrations, respectively. Each map is 200 μm × 200 μm. The correlations between the Fe–Ni and Fe–Cl fluorescence signals are shown in graphs (a) and (b), respectively. Each point on the graph represents the composition of one 5 μm × 5 μm pixel in the XFM.

Fig. 4 and HD in Fig. 5) is clearly visible from inspection of the XFM. The Ni and Fe XFM are nearly identical for the charged sample (HC) whereas there appears to be little similarity between the two maps for the discharged sample (HD). Plots of the Fe–Ni dependencies for charged sample (HC) shows strong positive and no correlation respectively, whereas the analogous plot for the discharged sample (HD) shows no correlation. Deeper analysis of the correlation dependence on Fe concentration is obtained by examining the correlation values in Table 2. For both the charged and discharged samples the Fe–Ni correlation values are larger in Fe-poor regions than in Fe-abundant regions. The Fe and Cl XFM for HC and HD samples show little similarity. The lack of Fe–Cl correspondence for these samples is also evident in the statistical analysis (Table 3) with the exception of the Fe-poor regions of the charged sample (HC).

The impact of the state of charge on the Fe–Ni elemental distribution in the low temperature samples (LC in Fig. 6 and LD in Fig. 7) is markedly less evident based on XFM alone. Comparison of the graphical analyses suggests a similar Fe dependence on Ni concentration for both charged and discharged samples. Examination of the correlation values in Table 2 indicates a strong positive Fe–Ni correlation in Fe-poor regions for both samples. The Fe and Cl XFM for the low temperature charged sample show little similarity whereas the same comparison for the discharged sample (LD) shows similar spatial distributions. The lack of Fe–Cl correlation in LC sample is also apparent in the correlation values (Table 3). In fact, the only appreciable Fe–Cl correlation for the low temperature samples is observed in Fe-poor regions of the discharged sample (LD).

In summary the charged state appears to lead to strong Fe–Ni spatial correlation at the high operating temperature and is insensitive of Fe concentration. However, at the low operating temperatures, the state of charge does not impact the Fe–Ni spatial correlation, suggesting that temperature is also an important variable. The state of charge does not appear to significantly influence Fe–Cl spatial correlation regardless of operating temperature.

3.2.1.2. Operating temperature. The data collected from the charged state samples indicated that the Fe elemental concentration was often correlated with that of Ni. The correlation was stronger in the HC sample which gave Pearson correlation values of $R = 0.780$ and 0.972 for Fe-rich and Fe-poor data respectively (Table 2). The corresponding values of $R = 0.243$ and 0.846 for the LC sample are lower, especially for Fe-abundant regions, suggesting that Fe and Ni have a greater tendency to be co-located at the higher temperature. Correlation coefficients between Fe and Cl concentration did not indicate a propensity for these elements to associate spatially in the charged samples. The strongest correlation ($R = 0.643$) was found in the Fe-poor parts of the higher temperature sample.

The discharged samples, HD and LD showed clear distinctions between the high and low temperature samples for both Fe–Ni and Fe–Cl elemental associations. The Fe–Ni and Fe–Cl plots of the high temperature (HD) sample (Fig. 5) display no significant correlations of Fe with either Ni or Cl, and gave a maximum correlation coefficient of 0.431. The analogous data for the low temperature sample show significantly stronger correlation of Fe with both Ni and Cl in the Fe-poor (but not Fe-rich) regions. We note the contrasting behavior of the Fe–Cl spatial correlation for Fe-poor regions within the samples examined here. At high temperature these elements are more strongly correlated in the charged (rather
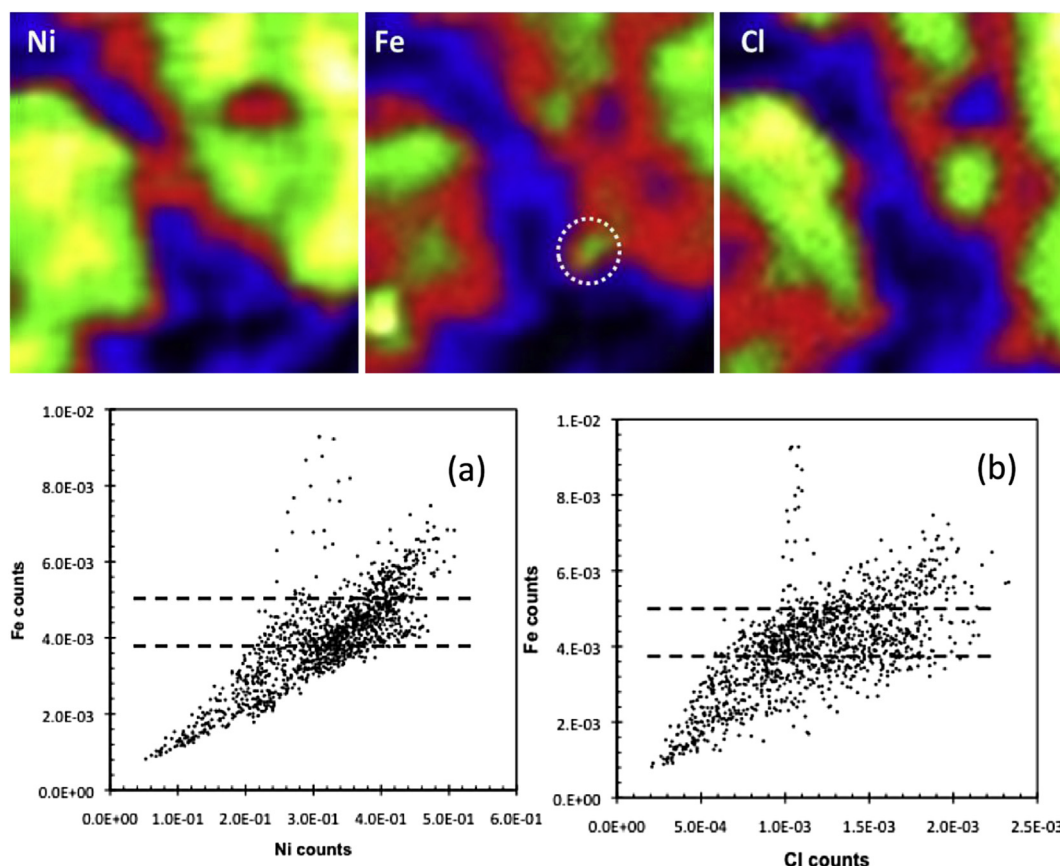
Fig. 7. XFM of LD cathode (240 °C, discharged) adjacent to BASE interface. The Ni, Fe, and Cl XFM are labeled correspondingly. White and black colors indicate high and low elemental concentrations, respectively. Each map is 200 μm × 200 μm. The correlations between the Fe–Ni and Fe–Cl fluorescence signals are shown in graphs (a) and (b), respectively. Each point on the graph represents the composition of one 5 μm × 5 μm pixel in the XFM.

than discharged) state, while the reverse is true at the lower temperature.

In summary, the higher cycling temperature leads to greater Fe–Ni elemental correlations in the charged state samples (HC and LC), particularly in Fe-abundant regions. In contrast, higher cycling temperature appears to have reduced Fe–Ni spatial correlation when comparing the discharged samples (HD and LD), particularly in Fe-poor regions. Fe–Cl correlations do not appear to have a systematic dependence on operating temperature.

3.2.1.3. Proximity to BASE interface. To evaluate the whether gradients in chemical properties, exist along the cathode, we compared the Pearson correlation values determined for the Fe–Ni and F–Cl elemental associations measured in regions of interest adjacent to BASE (see Tables 2 and 3) and current collector interfaces (see Supplemental information) for the four samples HC, HD, LC and LD using Meng's *z*-test for correlated correlations [27]. We found no consistent correlation between the proximity to the BASE or CC interface and Fe–Ni or Fe–Cl elemental associations

suggesting that the cathode is chemically homogeneous at the scale of our X-ray measurements.

3.2.2. XANES analysis

Ni and Fe oxidation states determined from XANES spectra were compared as a function of operating temperature and charge state. Fig. 8 shows the Ni and Fe oxidation state, expressed as % $NiCl_2$ and % Fe(II)-chloride, respectively, at both of the ZEBRA battery operating temperatures we tested. These data show that Ni is more oxidized in the charged samples (HC and LC) than the discharged samples (HD and LD) at both operating temperatures whereas for Fe this trend is only clearly evident at 240 °C. Additionally it can be seen that both Ni and Fe are present with higher oxidation states (on average) at 280° than at 240 °C. Note that the observed upper limit of 30% $NiCl_2$ is consistent with known ZEBRA battery chemistry where approximately 30% of the Ni metal is converted to $NiCl_2$ in the cathode and the remaining 70% of the Ni remains as Ni metal to create a conduction pathway to the current collector [22]. Whether the observed range of Fe(II)-chloride formation between

Table 2
The correlation values between Fe and Ni near BASE interface. Correlations considered statistically non-significant are shown in italics.

Sample	Correlation Fe-rich	*P*-value	Correlation Fe-poor	*P*-value
HC	0.780	<0.001	0.972	<0.001
HD	*0.028*	*0.571*	0.431	<0.001
LC	0.243	<0.001	0.856	<0.001
LD	*0.064*	*0.233*	0.859	<0.001

Table 3
The correlation values between Fe and Cl near BASE interface. Correlations considered statistically non-significant are shown in italics.

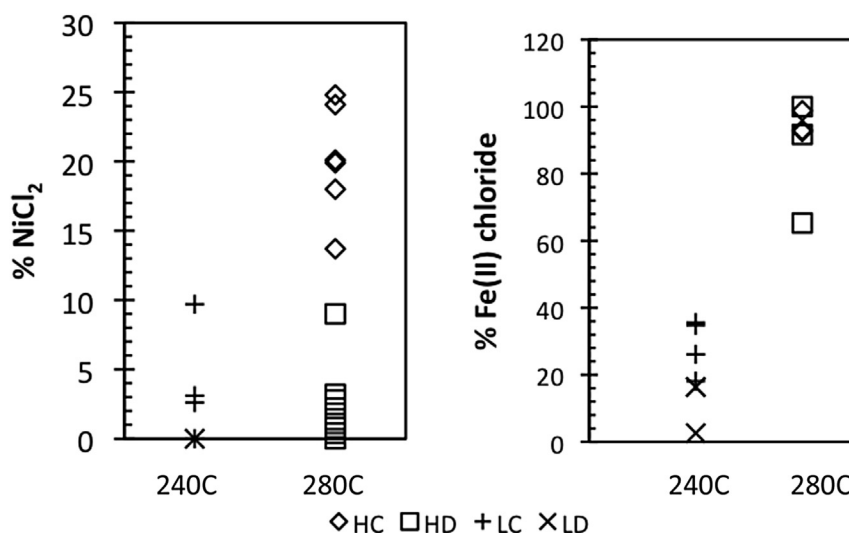| Sample	Correlation Fe-rich	*P*-value	Correlation Fe-poor	*P*-value
HC	0.099	0.013	0.643	<0.001
HD	0.309	<0.001	0.153	0.002
LC	*0.334*	*0.052*	*0.052*	*0.239*
LD	0.152	0.004	0.651	<0.001

Fig. 8. Ni and Fe oxidation estimates from XANES measurements. Both Fe and Ni are consistently more oxidized at 280 °C operating temperature than 240 °C. Additionally, for either operating temperature the samples in the charged state (HC and LC) are more oxidized than the discharged state (samples HD and LD).

0 and 100% reflects the actual Fe chemistry is less certain due to our choice of Fe standards (see section 2.4.4 and Supplementary information). We estimate the uncertainty at high Fe(II) chloride range is about 15%. Nonetheless XANES analysis demonstrated two clear findings 1) Fe is electrochemically active during battery cycling and 2) operational temperature has significant influence on the fraction of elemental metal that is oxidized during cycling.

3.2.3. Two dimensional XANES mapping

Both EDS and XFM measurements are somewhat limited in that they provide a spatial map of the elemental concentrations without providing speciation or oxidation states of elements of interest. As traditionally applied XANES provides this important information but located at a spot. Collection of the full XANES spectrum for a two dimensional map would be time prohibitive. We apply an X-ray absorption imaging technique described in section 2.3.2 to map the distribution of $NiCl_2$ in two regions near the BASE and current collector interface of the HC cathode. The resulting map of the $NiCl_2$ distribution of a 250 μm × 250 μm region near the charge collector interface is shown in Fig. 9B. The red regions are correlated with the presence of $NiCl_2$, while blue regions are correlated with the presence of Ni metal. No significant difference in $NiCl_2$ distribution was observed for a similar region located adjacent to the BASE interface. We note that regions of higher $NiCl_2$ concentration identified in these maps correspond to regions of low total Ni, or more intuitively, regions of high total Ni are associated with Ni metal. We also used an alternative method of relying on the Ni to Cl elemental ratios from XFM to map Ni metal and $NiCl_2$ distribution (shown in Fig. 9C). This alternate approach can be misleading in a complex system due to the likely presence of the additional chloride-containing phases such as $NaAlCl_4$, Fe(II)-chloride and NaCl.
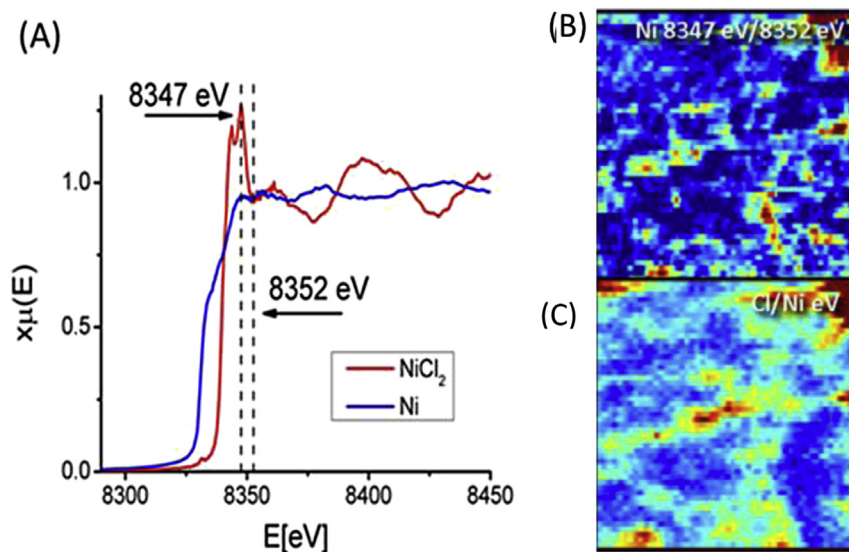

Fig. 9. Spatial distribution of $NiCl_2$ in HC cathode. Ni K-edge XANES are shown in (A). The vertical lines at 8352 and 8347 eV are the incident X-ray energies at which the XFM maps were collected adjacent to the current collector. The top map (B) shows the intensity ratio collected at the two energies, which is a measure of the quantity of $NiCl_2$ present. This may be compared to the lower map (C) which plots the Cl/Ni ratio.

4. Conclusions

We have used complementary X-ray absorption techniques—XFM, XANES, and XANES chemical mapping to probe the Ni and Fe chemical speciation within two sets of chemically identical ZEBRA batteries cycled at two different temperatures. We have found that operating temperature and charge state influences whether Fe concentration at each location correlates with Ni or Cl concentration, whereas proximity to the BASE interface does not. We also observe that a positive correlation of Fe with either Ni or Cl is strongest in regions of the cathode where the total concentration of Fe is relatively low. In Fe-abundant regions the correlation coefficients ranged between non-significant, positive and negative values.

The chemical speciation is largely determined by operating temperature and charge state. The XANES analysis suggests that there are primarily only two species of Ni and of Fe respectively—namely the metal and chloride phases. XANES also confirms that oxidation and reduction of both Ni and Fe species is occurring during cycling. Additionally, the XANES data suggests that the reduction of the Ni and Fe is more complete in the discharge state at the higher cycling temperature, which would be beneficial in providing higher energy capacity. While these measurements add to the understanding of the behavior of Fe additives in the ZEBRA battery system, further measurements spanning a range Fe concentration are needed to provide a more comprehensive and reliable interpretation. We have demonstrated the potential of XANES mapping as a tool for developing a more complete understanding of the role of additives in specific batteries.

Acknowledgments

Appendix A. Supplementary data

Supplementary data related to this article can be found at http://dx.doi.org/10.1016/j.jpowsour.2013.08.046.

References

[1] B. Hayman, J. Wedel-Heinen, P. Brøndsted, MRS Bull. 33 (2008) 343–353.
[2] D. Ginley, M.A. Green, R. Collins, MRS Bull. 33 (2008) 355–364.
[3] B.S. Lee, D.E. Gushee, Chem. Eng. Prog. 104 (2008) S29–S32.
[4] Z. Yang, J. Zhang, M.C.W. Kintner-Meyer, X. Lu, D. Choi, J.P. Lemmon, J. Liu, Chem. Rev. 111 (2011) 3577–3613.
[5] Electrical-Storage-Association, http://www.electricitystorage.org/ESA/technologies/.
[6] J.T. Kummer, in: J.O.M.H. Reiss (Ed.), Beta-Alumina Electrolytes, Pergamon Press, 1972, pp. 141–175.
[7] J.L. Sudworth, A.R. Tilley, The Sodium Sulphur Battery, Chapman & Hall, London, 1985.
[8] X. Lu, G. Xia, J.P. Lemmon, Z. Yang, J. Power Sources 195 (2010) 2431–2442.
[9] Z. Wen, Z. Gu, X. Xu, J. Cao, F. Zhang, Z. Lin, J. Power Sources 184 (2008) 641–645.
[10] R.C. Galloway, J. Electrochem. Soc. 134 (1987) 256–257.
[11] R.J. Bones, D.A. Teagle, S.D. Brooker, F.L. Cullen, J. Electrochem. Soc. 136 (1989) 1274–1277.
[12] R.J. Bones, J. Coetzer, R.C. Galloway, D.A. Teagle, J. Electrochem. Soc. 134 (1987) 2379–2382.
[13] P.T. Moseley, R.J. Bones, D.A. Teagle, B.A. Bellamy, R.W.M. Hawes, J. Electrochem. Soc. 136 (1989) 1361–1368.
[14] P. Parthasarathy, N. Weber, A.V. Virkar, ECS Trans. 6 (2007) 67.
[15] X. Lu, G. Li, J.Y. Kim, J.P. Lemmon, V.L. Sprenkle, Z. Yang, J. Power Sources 215 (2012) 288–295.
[16] X. Lu, G.W. Coffey, K.D. Meinhardt, V.L. Sprenkle, Z. Yang, J.P. Lemmon, ECS Trans. 28 (2010) 7.
[17] X. Lu, J. Lemmon, V. Sprenkle, Z. Yang, JOM J. Miner. Met. Mater. Soc. 62 (2010) 31–36.
[18] B.V. Ratnakumar, A.I. Attia, G. Halpert, J. Power Sources 36 (1991) 385–394.
[19] L. Redey, D.R. Vissers, J. Prakash, U.S. Patent Office, 5,283,135; 5,340,668, 1994.
[20] J. Prakash, L. Redey, D.R. Vissers, J. Electrochem. Soc. 147 (2000) 502–507.
[21] R.C. Galloway, S. Haslam, J. Power Sources 80 (1999) 164–170.
[22] J.L. Sudworth, J. Power Sources 100 (2001) 149–163.
[23] M. Hosseinifar, A. Petric, J. Power Sources 206 (2012) 402–408.
[24] X. Lu, B.W. Kirby, W. Xu, G. Li, J.Y. Kim, J.P. Lemmon, V.L. Sprenkle, Z. Yang, Energy Environ. Sci. 6 (2013) 299–306.
[25] B. Ravel, M. Newville, J. Synchrotron Radiat. 12 (2005) 537–541.
[26] J.P. Shaffer, Annu. Rev. Psychol. 46 (1995) 561–584.
[27] X.L. Meng, R. Rosenthal, D.B. Rubin, Psychol. Bull. 111 (1992) 172.